Received: 4 August 2020 | Revised: 20 December 2020 | Accepted: 23 December 2020

DOI: 10.1002/vzj2.20109

Vadose Zone Journal

SPECIAL SECTION: AGROGEOPHYSICS: GEOPHYSICS TO INVESTIGATE SOIL–PLANT–ATMOSPHERE INTERACTIONS & SUPPORT AGRICULTURAL MANAGEMENT

Hydrodynamic characterization of soil compaction using integrated electrical resistivity and X-ray computed tomography

Mihai O. Cimpoiaşu[1,2] | **Oliver Kuras**[2] | **Paul B. Wilkinson**[2] | **Tony Pridmore**[3] | **Sacha J. Mooney**[1]

[1] Division of Agriculture and Environmental Sciences, School of Bioscience, Univ. of Nottingham, Sutton Bonington, Leicestershire LE12 5RD, UK

[2] Geophysical Tomography Team, British Geological Survey, Keyworth, Nottinghamshire NG12 5GG, UK

[3] School of Computer Science, Univ. of Nottingham, Wollaton Road, Nottingham, Nottinghamshire NG8 1BB, UK

Correspondence
Mihai O. Cimpoiaşu, British Geological Survey, Keyworth, Notthinghamshire, UK.
Email: mcim@bgs.ac.uk

Assigned to Associate Editor Ulrike Werban.

Abstract

Modern agricultural practices can cause significant stress on soil, which ultimately has degrading effects, such as compaction. There is an urgent need for fast, noninvasive methods to characterize and monitor compaction and its impact on hydraulic processes. Electrical resistivity tomography (ERT) is a well-established method used for the assessment of soil hydraulic properties due to its high temporal resolution and sensitivity to changes in moisture content and salinity, whereas X-ray computed tomography (CT) can be used for high-spatial-resolution imaging of soil structure. We used the combined strengths of both methods to study soil under three different levels of compaction. The soils were X-ray scanned and electrically monitored after the application of a saline solution to the soil surface. The scans revealed the pore network architecture and allowed us to compute its size and connectivity. The ERT models revealed inhibited percolation rates for soils with a lower bulk density, but also how resistivity changes are spatiotemporally distributed within the soil columns. Furthermore, we obtained a quantitative link between the two methods, by which voxels more densely populated with pores were associated with higher temporal variations in electrical resistivity. Building on this, we established a spatial collocation between pore structure and distribution of solution during percolation. This demonstrates the potential of the combined strengths of the two tomographic methods to obtain an enhanced characterization of soil hydrodynamic properties.

1 | INTRODUCTION

With an increasing agricultural demand worldwide and pressure from population increase and a changing climate, there is an urgent need for fast, robust, and noninvasive methods of soil assessment. Due to the intensive use of heavy machinery, soil structure degradation in the form of compaction has become a serious problem (Hamza & Anderson, 2005). Classical invasive soil sampling methods often require significant manual labor and alteration of soil's natural properties (e.g., structure) and have difficulties in measurement repeatability (Furman, Arnon-Zur, & Assouline, 2013). Other practices that make use of minimally invasive sensors, such as time domain reflectometry (TDR), have a good temporal resolution, but lack site spatial coverage (Furman et al., 2013).

Abbreviations: CT, computed tomography; ERT, electrical resistivity tomography; 3D, three-dimensional; TS, time step; WS, Waxman–Smits.

Electrical resistivity tomography (ERT) is a noninvasive, quick, and relatively easy-to-use method of monitoring changes in soil bulk electrical resistivity, a proxy for changes in soil properties such as pore fluid content, soil texture, pore structure, saturation, pore fluid salinity, and so on (Samouëlian, Cousin, Tabbagh, Bruand, & Richard, 2005). The coverage it provides allows it to be applied to large-scale field studies (Michot, Dorigny, & Benderitter, 2001) and on smaller scale laboratory investigations of root zone properties (Garré, Javaux, Vanderborght, Pagès, & Vereecken, 2011). Electrical resistivity tomography produces tomograms of the subsurface by fitting a predicted model of the subsurface resistivity distribution to measured electrical resistance (a mathematical technique called inverse modeling). Romero-Ruiz, Linde, Keller, and Or (2018) identifies electrical resistivity methods as valuable for the study of soil compaction due to the amount of information regarding soil properties it can reveal. However, finding the best fit resistivity model is challenging as the ERT inverse problem is nonunique and ill conditioned. Therefore, the information it provides needs careful treatment and interpretation. A priori information about the medium surveyed with ERT can be used to constrain the inversion in order to produce stable unique solutions (Loke, Chambers, Rucker, Kuras, & Wilkinson, 2013). In this context, ERT was previously used to study soil properties in conjunction with other soil assessment methods. Michot et al. (2001), at field scale, used minimally invasive TDR sensors, which provide point measurements of water content to ground truth observations made on ERT tomograms. Also, in a laboratory study on soil columns, Garré et al. (2011) used TDR sensors in order to validate water mass balance calculated by ERT and minirhizotrons to obtain images of root development. However, such point sensors lack spatial resolution and do not have the three-dimensional (3D) capability of ERT; therefore, a complete conjunctive assessment of the entire soil volume is not obtained. Another complementary method is ground-penetrating radar (GPR), used for its ability to delineate soil stratigraphic boundaries, which can in turn be used to constrain and explain the electrical resistivity profile (Musgrave & Binley, 2011). Electromagnetic induction method (EMI) was used for its capability of mapping soil electrical conductivity at the field scale (1–10 ha) and beyond (Cockx, Van Meirvenne, & De Vos, 2007), but does not have a good vertical penetration, hence was combined with ERT for a joint characterization of aquifers (Linde, Binley, Tryggvason, Pedersen, & Revil, 2006) or soil hydraulic conductivity (Farzamian, Monteiro, & Khalil, 2015). However, differences in dimensionality, between ERT and aforementioned methods, and inherent limitations do not allow the collocation between soil parameters measured.

X-ray computed tomography (CT) is a well-established noninvasive method that has been used in the soil sciences for assessing soil structure in 3D at very high resolutions (10 μm) (Tracy et al., 2015). A further benefit of X-ray CT is that it allows the visualization and a quantitative assessment of pore architecture, which in turn can be used to estimate soil hydraulic properties (Anderson, Wang, Peyton, & Gantzer, 2003; Grayling et al., 2018). On this basis, Cimpoiaşu, Kuras, Pridmore, and Mooney (2020) identified the complementary potential of X-ray CT-derived information to enhance the understanding of geoelectrical studies of root zone processes. There are few studies to date using ERT and X-ray CT in conjunction for the study of soil processes. Olsen, Binley, and Tych (1999) used the two methods to characterize solute transport in soils, but the linkage between the two methods was purely qualitative. Cassiani, Kemna, Villa, and Zimmermann (2009), in a study on soil columns, used X-ray CT scanning to reveal that a non-aqueous-phase liquid distribution after injection in soil was the source of DC signal variability and not the chemical interactions. Both X-ray CT and ERT have the capability to operate in 3D, which allows us to collocate the soil properties assessed over the appraised soil volume. However, X-ray CT lacks high temporal resolution, as the acquisition of a complete 3D scan sequence depending of the level of detail required can take several hours. However, most modern systems are able to scan more quickly (e.g., in minutes rather than hours).

According to Wildenschild and Sheppard (2013), 3D imaging of macropore architecture in combination with real-time measurements of solute transport has the potential to advance knowledge of solute flow. In this study, we aimed to formulate an improved characterization of the effect soil compaction has on hydrodynamic behavior using a combined imaging approach utilizing the specific strengths of the two tomographic methods mentioned above. Firstly, X-ray CT scanning was performed on soils to resolve the parametric differences in pore structure associated with differences in bulk density. Secondly, ERT was used to monitor the infiltration of a saline solution through the same soil columns. By this approach, we aimed to associate the soil solution percolation rates with soil structural parameters affected by the soil bulk density. Furthermore, we demonstrate that datasets from the two tomographic methods can be quantitatively collocated in

Core Ideas

- ERT monitors near real-time solution percolation in soils with different bulk densities.
- X-ray CT images pore network changes in connectivity with increasing bulk density.
- Density of the pore network is spatially collocated with bulk electrical resistivity.
- Time-lapse solution percolation through soils is explained in the context of localized porosity.

TABLE 1 Values of structural parameters corresponding to specific soil columns measured in the laboratory (bulk density [BD]) and estimated from X-ray images (porosity [ϕ], pore size [PS], and connectivity density [ConD])

Sample group	Sample no.	BD	ϕ	PS	ConD
		Mg m^{-3}	%	mm^2	mm^{-3}
G1	1	1.39	13.66	0.31	34,027
	2	1.39	12.25	0.58	31,331
	3	1.36	10.69	0.69	25,282
G2	1	1.44	8.19	1.63	14,757
	2	1.49	7.05	0.15	12,520
	3	1.44	8.21	0.71	15,086
G3	1	1.54	4.37	0.31	11,534
	2	1.54	5.55	0.69	11,659
	3	1.64	1.97	0.11	9,662

order to expose the 3D spatial distribution link between levels of porosity (from CT) and changes in electrical resistivity.

2 | MATERIALS AND METHODS

2.1 | Soil sampling

We collected 18 undisturbed soil columns from random locations in an experimental field of the same soil type at the University of Nottingham experimental farm at Bunny, Nottinghamshire, UK (52°51′21″ N, 1°07′31″W). The soil was a clay textured (40% clay, 25% silt, and 35% sand) Orthic Luvisol from the Worcester series (coarse-loamy, mixed, superactive, frigid Argic Endoaquods). Before sampling, the top few centimeters of soil were removed in order to insure a good contact between the cylinder and the soil's surface. Plastic cylinders (6.8-cm diam., 14-cm height) were gently inserted into the topsoil to 20-cm depth and were extracted by careful removal of the surrounding material. This depth was chosen because its proximity to the surface makes it more prone to be affected by compaction. Inside the cylinder, the height of the soil column was 12.5 cm. On return to the laboratory, the samples were assessed on their bulk density, and nine columns were attributed to three equal sized groups (G) that corresponded to the following intervals: 1.3–1.4 Mg m^{-3} (G1); 1.4–1.5 Mg m^{-3} (G2), and 1.5–1.65 Mg m^{-3} (G3) (Table 1), prior to storage at 4 °C before experimentation. As the aim was to obtain three groups of samples with distinctive bulk densities, the remaining nine columns were not considered for further analysis.

2.2 | Saline solution infiltration

For the solute infiltration experiment, we chose one column from each group (G1–G3) with a bulk density closest to the group's average (1.38, 1.43, and 1.57 Mg m^{-3} for G1, G2, and G3, respectively). The underlying assumption was that samples with a similar bulk density and X-ray-derived porosity show similar hydraulic conductivity estimates to Anderson et al. (2003); thus, only one column from each group was used for subsequent ERT monitoring. Prior to the start of infiltration, each soil column was modified in order to accommodate electrical measurements. Twenty-four stainless steel electrodes were fitted around the circumference of the plastic sleeve in three equally spaced rows of eight (Figure 1). Custom-made caps were designed for the cylinders in order to accommodate the input and output of the saline solution. The top cap extended inside the cylinder to occupy the remaining 1.5 cm left between the soil and the cylinder's edge. Firstly, using a peristaltic pump, the samples were slowly saturated (5×10^{-9} m^3 s^{-1}) with deionized (DI) water from the bottom up in order to remove the air from the sample. The infiltration speed was maintained throughout the whole experiment. Secondly, a 0.01 M KCl (0.13 S m^{-1}) solution was infiltrated until a steady state was reached (decided upon the evolution of effluent's conductivity). These first two phases lasted 24 h each. Finally, a much more conductive 0.05 M KCl (0.53 S m^{-1}) solution was infiltrated, which acted as a tracer. As the pore solution reached the top of the sample, the effluent was collected and its electrical conductivity recorded with an EM50 data logger.

2.3 | ERT monitoring and inversion

Electrical resistivity tomography is a near-surface geophysical method that uses electrical resistance measurements in order to reconstruct an image of the bulk electrical resistivity of the subsurface. Electrical currents are injected into the ground and the resulting electrical potential difference is recorded. Resistivity (Ω m, or its inverse, conductivity [σ]) is obtained using Ohm's law:

$$\rho = K R = K \frac{\delta V}{I} \quad (1)$$

where R (Ω) is the electrical resistance, I (A) is the injected current, δV (V) is the electrical potential difference, and K is the geometric factor, which depends on the geometric arrangement of electrodes.

During the final stage of the infiltration, transfer resistance measurements were continuously collected, in dipole–dipole configurations, using a GEOLOG2000 GeoTom MK-RES/IP/SP. Air temperature was maintained constant at 21 °C throughout the experiment. One complete pair of measurement sequences, comprising normal (R_n) and reciprocal (R_r) configurations (where current and potential electrodes are switched (LaBrecque, Miletto, Daily, Ramirez, & Owen, 1996), contained 772 measurements and took approximately

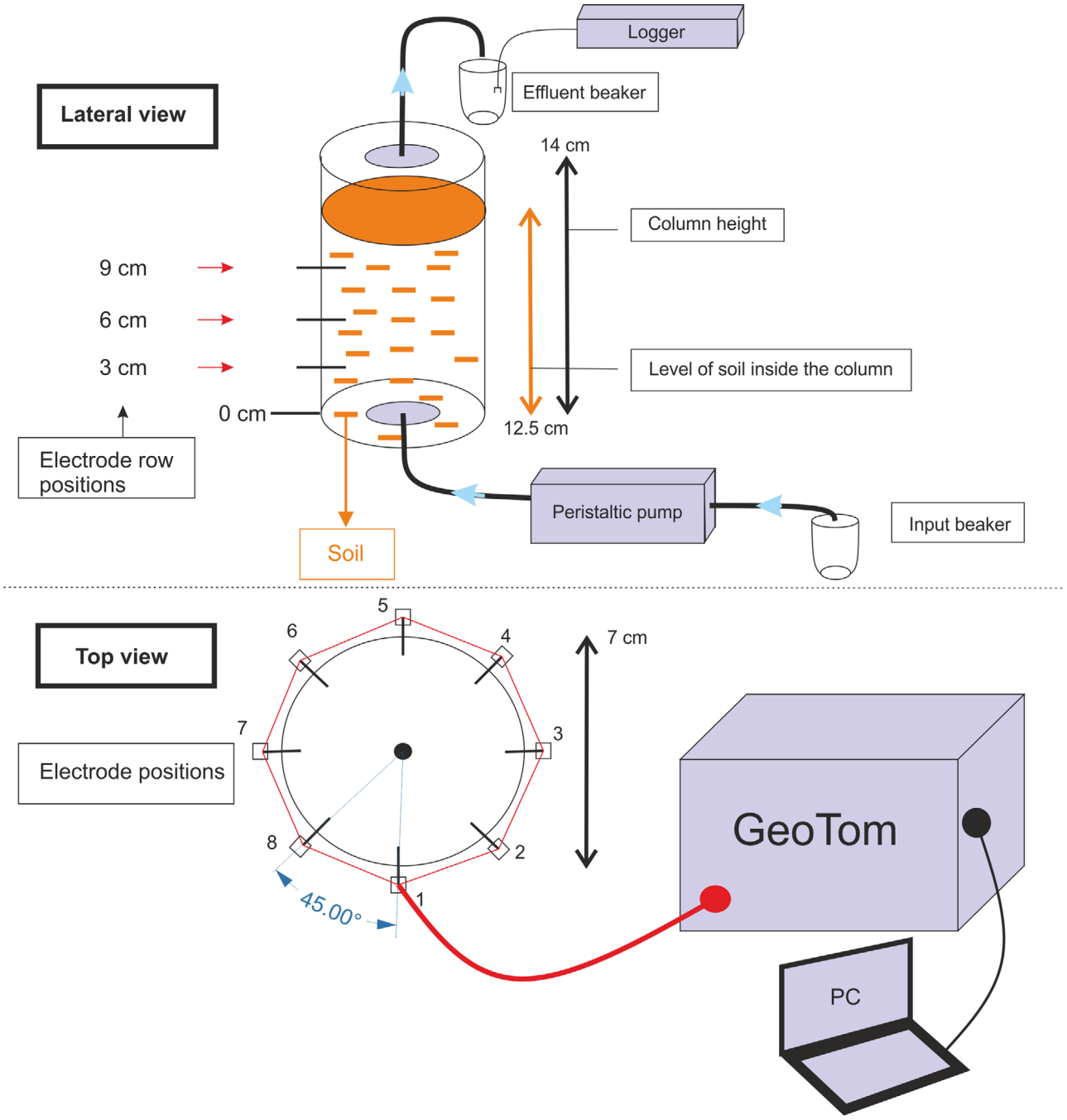

FIGURE 1 Schematic of the laboratory soil column experiment. Lateral view: KCl solution infiltration setting. Top view: electrode arrangement for electrical resistivity tomography (ERT) monitoring

15 min. A measurement sequence used all possible combinations of dipoles on individual rows (288) and cross-row equatorial dipoles (484). A complete measurement sequence is available upon request. The transfer resistance value subsequently used was the pair's mean R_m and its associated standard error, referred to as the reciprocal error E_r, was defined as:

$$|E_r| = 100\left(\frac{|R_r - R_n|}{R_r - R_m}\right) \quad (2)$$

Firstly, measurements with a reciprocal error >5% were discarded. Secondly, in an attempt to obtain more robust error estimates, and following the approach described in Mwakanyamale, Slater, Binley, and Ntarlagiannis (2012), data with similar transfer resistances was binned and subsequently an error model was fitted to the reciprocal error average corresponding to each bin. This model was used to estimate the final error associated with each measurement.

After data acquisition, for every column, we obtained 32 distinct datasets of apparent resistivity corresponding to 32

different time steps (TSs). In order to obtain a model of electrical resistivity, an inversion algorithm was used, in which a starting resistivity model is iteratively adjusted in order to achieve the best fit with the measured apparent resistivity values. For inversion and design of the 3D structural mesh model, E4D inversion software (Johnson, Versteeg, Ward, Day-Lewis, & Revil, 2010) was used, which uses an Occam-type inversion. It produces an image of M voxels of electrical resistivities (ρ_i with $i = 1,2, \ldots, M$) given a set of N four electrode resistances (R_j [Ω] with $j = 1,2, \ldots, N$) by minimizing the objective function Ψ:

$$\Psi = ||W_\varepsilon[\mathbf{d} - f(\mathbf{m})]||_2^2 + \lambda||\mathbf{W}_s[\mathbf{m} - \mathbf{m}_0]||_2^2 \quad (3)$$

where **d** is the data vector, **m** is the model given by the parameters of the inversion $m_j = \log(\rho_j)$ (Ω m), $f(\mathbf{m})$, is the forward model for parameters **m**, $\mathbf{m_0}$ is a homogeneous starting model vector, W_ε is a smoothing operator, λ is the regularization parameter that determines the amount of smoothing imposed on **m**, and $\mathbf{W}_s$ is an error weighting matrix. We acknowledge the importance of choosing appropriate regularization parameters for accurate inversion results (Rao, Lesparre, Orozco, Wagner, & Javaux, 2020). After a series of synthetic model simulations, we concluded that 100 is an appropriate value for λ. To provide a mesh, we used Tetgen (Hang, 2015), a mesh generator incorporated in E4D. We designed a cylindrical volume made up of 5,492 unstructured tetrahedra refined around the position of the electrodes. We considered electrodes as points in our mesh model, which we acknowledge can cause issues in small-scale resistivity imaging. However, when electrodes protruded the sample, they did so for no more than 0.5 cm, which is below 20% of electrode separation, an acceptable threshold for point electrodes to be considered according to Rücker and Günther (2011).

By comparing the resistivity distribution between different TSs, we can estimate the resistivity change over time across the soil volume. Resistivity inversion is an ill-posed problem (Hansen, 1992), and the resulting models carry inherent limitations such as solution nonuniqueness. This implies that multiple models fit the data to the same degree of accuracy, hence choosing the "correct" model is a challenge both conceptually and practically. Therefore, for our soil samples, the inversion model results are only an indication of the resistivity variation over time. Furthermore, since electrical resistivity is influenced by many factors depending on both soil properties (e.g., porosity, clay content, water content) and experimental setup (e.g., contact impedance, electrode layout), there is no certainty that the source of such variation is indeed the change in pore solution salinity determined by the infiltration of a more conductive solution.

2.4 | X-ray computed tomography and image processing

X-ray CT allows visualization of the interior structure of a target object due to the attenuation properties of electromagnetic waves. X-rays are produced in a tube containing an anode and a cathode when a voltage is applied across the electrodes. The Beer–Lambert equation describes the X-ray beam attenuation as it passes through a target medium (Wildenschild, Hopmans, Vaz, Rivers, & Rikard, 2002):

$$\mathrm{IN} = \mathrm{IN}_0 \exp(-\mu D) \quad (4)$$

where D (m) is the thickness, μ (m^{-1}) is the attenuation coefficient, and IN_0 and IN are the intensities before and after passing through the sample.

In our experimental setting, the sample rotates and the source–detector pair is fixed to allow projections from different angles. The angle increment of the projector is given by the number of image radiograms obtained per sample—in our case, 2,400. All columns were scanned with a V|Tome|x M X-ray scanner (scan settings: 140 kV, 160 μA, 2,400 images, skip [number of images ignored as the sample moves to a new location in order to improve stabilization; du Plessis, Broeckhoven, Guelpa, & le Roux, 2017]/average [number of images taken at each location to produce an averaged final image] 1/0, 8-min scan time, and 40-μm resolution] at the Hounsfield Facility, University of Nottingham, Sutton Bonington, UK.

X-ray CT is widely regarded as a noninvasive method of soil assessment (Duliu, 1999). This is because the sample's integrity is not altered during image data acquisition. On the other hand, during sampling, the soil is removed from its natural environment, hence discontinuing matter and energy exchanges. However, in our study, we are applying X-ray CT to look at the physical structure of the pore network, which we consider partly because we took necessary precautions (e.g., meticulous sampling, refrigeration) not to have been altered during sampling or by other biogeochemical processes that followed in the short time up to the scanning day.

The radiograms obtained were digitally reconstructed using datos|x and processed using the Volume Graphics 2.2 software, over an 8-bit value range. For the 3D representation of a soil column volume, stacks of cross-sectional images were imported. Further image processing was performed using the open source program ImageJ (Schindelin et al., 2012). A representative subvolume of 3.8 × 3.8 × 6 cm^3 (Figure 2) was selected in order to exclude areas adjacent to the sample edges, which might have been subjected to physical disturbance during extraction. One pass of two process filters (sharpen and median) was applied to this subvolume in order

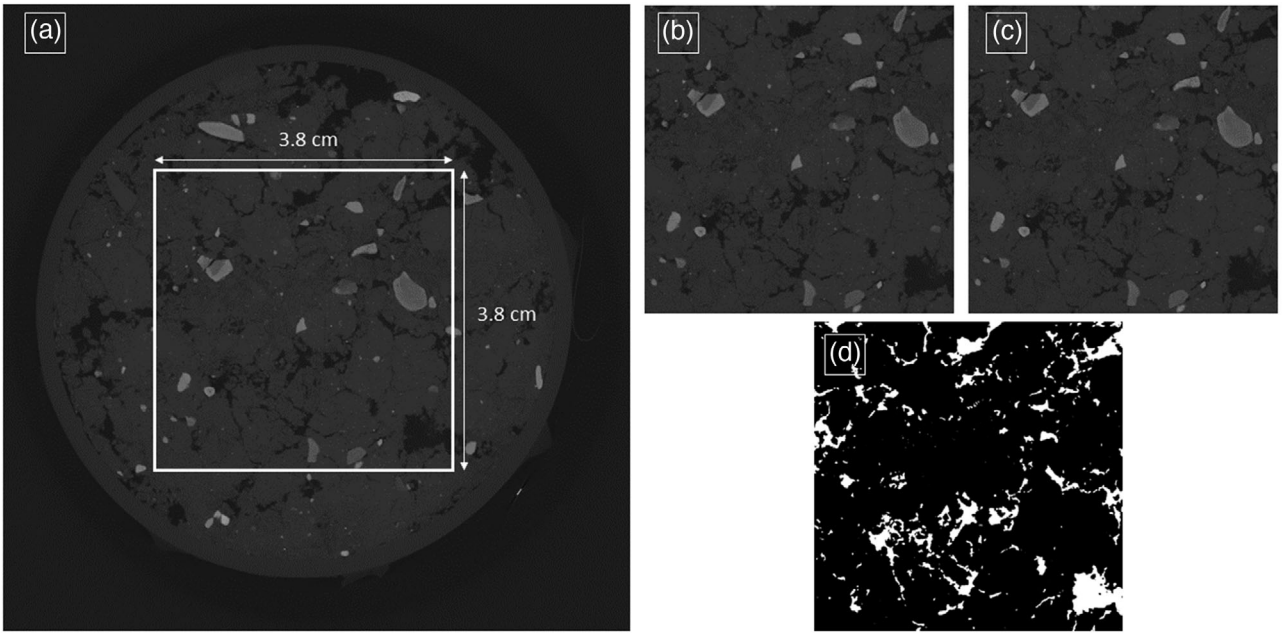

FIGURE 2 Images of the soil volume reconstructed post scanning. (a) Top view cross-section and the representative area selected for further image processing. (b) Selected area after being cropped from the cross-sectional image. (c) Selected area after sharpen and median filters were applied. (d) Selected area after the Otsu threshold was applied in order to segment the pore space

to improve image quality before segmentation, which was assessed by inspection of the grayscale histogram. Afterwards, an Otsu threshold (Otsu, 1979) was applied in order to binarize the images and segment the air-filled pore space represented by low grayscale values indicative of low absorption (Figure 2d). This sequence of image processing steps was establish empirically in order to obtain an accurate separation between air-filled pore space and the rest of the soil volume. The segmented images were finally collated into a binarized 3D soil volume. By further calculating the proportion of white pixels from the whole volume, an estimate for total air-filled porosity (hereby referred to as porosity) was obtained. By computing the volume of the individual white voxels (Figure 2d), an estimate of the individual pore size was obtained. We acknowledge that at the current operating resolution (i.e., 40 μm), we can only observe macropores. Furthermore, in the attempt of computing the pore size distribution, we considered the cumulative volume comprised by pores of eight size classes (40–250, 250–500, 500–750, 750–1,000, 1,000–1,250, 1,250–1,500, 1,500–1,750, 1,750–2,000 μm). We define the cumulative volume as the total volume occupied by summing pore volumes of a specific size. Also, by using BoneJ (Doube, Kłosowski, Arganda-carreras, & Fabrice, 2010), a plugin for ImageJ, we obtained an estimate for the pore connectivity density (ConD) as follows:

$$\mathrm{ConD} = \frac{1 - \Delta X}{Ah} \tag{5}$$

where ΔX is the sample's contribution to the Euler characteristic (a number that describes a topological space's shape or structure (Odgaard & Gundersen, 1993), A (m^2) is the area of the image, and h (m) is the height of the image stack.

Finally, in order to establish if there was a statistically significant difference between groups (G), we used a one-way ANOVA test within Python 3.6 package 'scipy-stats.'

2.5 | Pedophysical model

Soil bulk electrical resistivity is a complex parameter that depends on many physicochemical properties. Archie (1942) was one of the first pedophysical relations formulated to describe electrical resistivity as a function of rock's porosity and fluid content [$f(\phi, \theta)$]. Building on Archie's relation, the Waxman–Smits (WS) model includes surface conductivity effects, which become important when an increased content of clay particles is present (Waxman & Smits, 1968):

$$\rho^{-1} = f(\phi,\ \theta,\ \sigma_f) = \phi^m \left(\frac{\theta}{\phi}\right)^n \left[\sigma_f + BQ_v \frac{\phi}{\theta}\right] \tag{6}$$

where ϕ is porosity, θ is pore fluid content, σ_f is pore fluid conductivity (S m^{-1}), B (m^2 s^{-1} V^{-1}) is an empirical equivalent counterion mobility factor at 25 °C, Q_v (cmol kg^{-1}) is the excess of surface charge of the solid phase per unit of pore volume, and m and n are dimensionless empirical parameters.

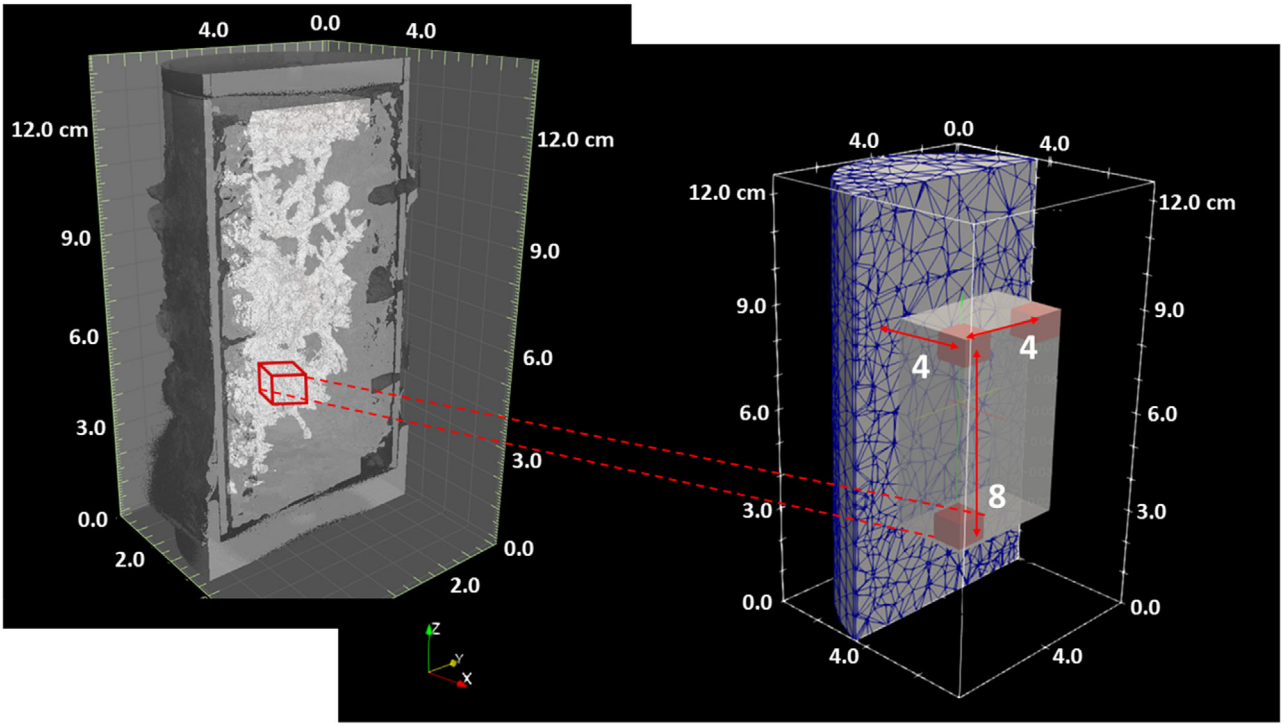

FIGURE 3 Left: Cross-sectional vertical clip of the X-ray computed tomography (CT) three-dimensional (3D) model of binarized soil. The white structure represents the air-filled pore space on which the surrounding soil in light gray was superimposed. Right: Mesh model used for resistivity inversion. The red cubes represent the voxel selection used to draw a quantitative relationship between the two datasets. White numerals 4, 4, and 8 indicate the number of red cubes used on respective axes. The opaque gray box encloses the sample subvolume subjected to quantitative analysis

Assuming the samples are fully saturated and using a X-ray CT-derived value of porosity, this relationship was used to translate between porosity and corresponding electrical resistivity. Ultimately, in order to express resistivity change, the fractional change between two resistivity values (ρ_i and ρ_j) corresponding to i the initial TSs of the infiltration and j a subsequent TS was computed:

$$\frac{\rho_j - \rho_i}{\rho_i} = \frac{f(\sigma_{f_j}) - f(\sigma_{f_i})}{f(\sigma_{f_i})} \tag{7}$$

With no other external factors acting on the samples, the underlying assumption was that the change in pore solution salinity will be the main contributor to the change in bulk soil electrical resistivity. Nonetheless, in an attempt to enhance the interpretation of the resistivity change exposed as a result of inversion, we used the X-ray CT pore structural parameters as a source of a priori information, such as porosity, pore size distribution, and pore connectivity density.

2.6 | Quantitatively link ERT and X-ray models

The ERT and X-ray model results essentially represent the distribution of electrical resistivity and X-ray absorption, respectively, for the same cylindrical volume. It is important to note that there is a considerable difference in spatial resolution between the two tomographic methods (mm to 40 μm). The selected subvolume was therefore divided into 128 equally sized voxels (4 × 4 × 8), and for every voxel (Figure 3), the average model cell change in electrical resistivity was estimated. Concurrently, the average porosity was computed for the corresponding voxel with the same position and dimension in the X-ray 3D pixel model. Finally, the voxel resistivity changes were binned into 5% intervals (starting at 10–15%), and the average resistivity change in each bin was calculated.

3 | RESULTS AND DISCUSSION

3.1 | ERT monitoring

We derived several models of bulk soil electrical resistivity corresponding to the different stages of infiltration (each sample at every TS had a corresponding model with the exception of the last two TSs of G1 due to a systematic error). Upon initial data filtering, not every TS retained the same number of quadrupoles. However, the retained measurement proportion was very high (an average of >92%) for every TS. Muller et al. (2010), demonstrated in a tracer

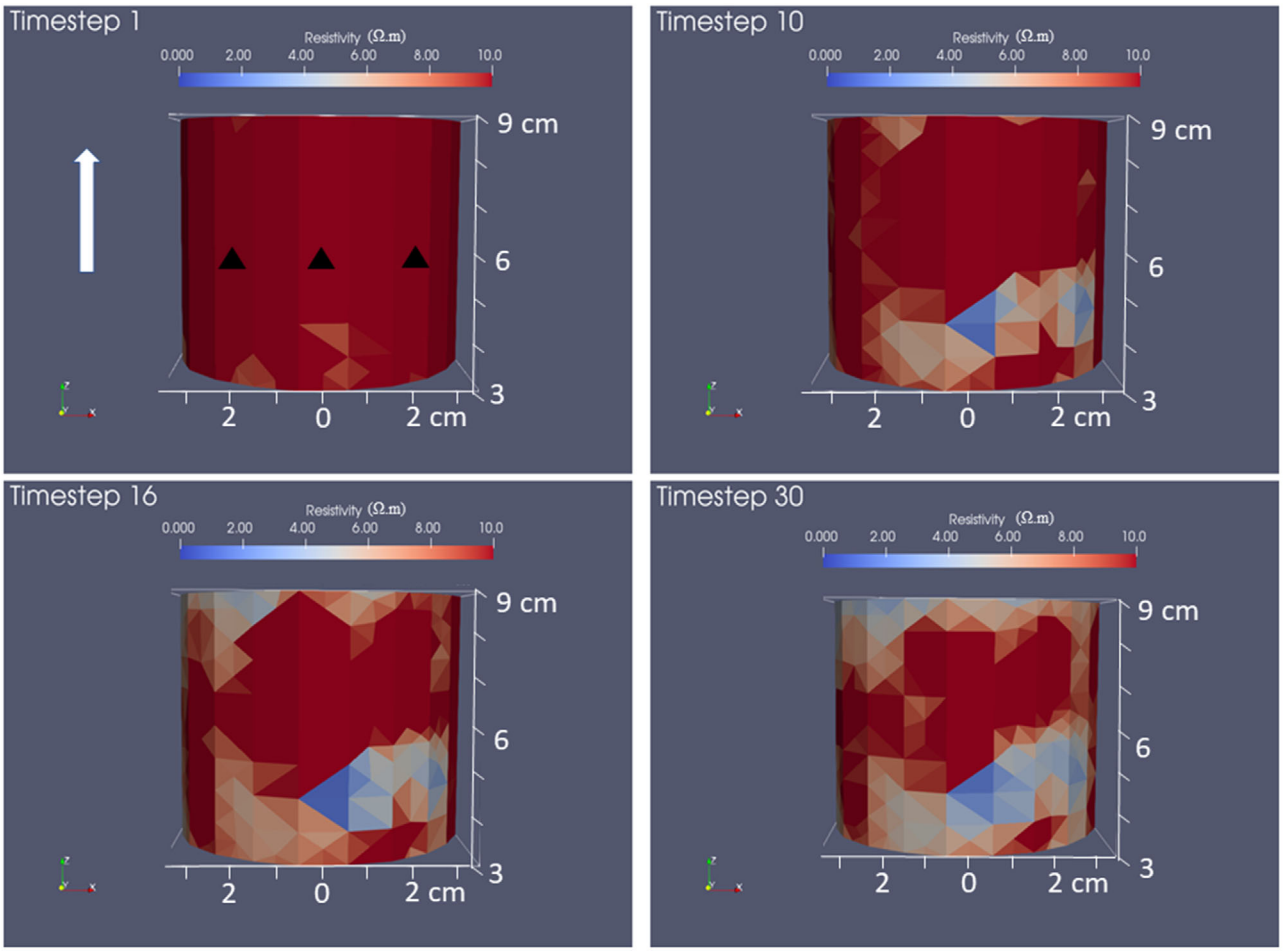

FIGURE 4 Clip of the G1 column resistivity model in four stages of the high-molarity solution infiltration. White arrow indicates flow direction (upward). Time steps (TSs) correspond to 15, 150, 240, and 450 min from the start of the high molarity (0.05 M) infiltration. The positions of the middle row electrodes (6 cm) visible from this view angle are marked by dark triangles in the top left image corresponding to TS 1

experiment that different ERT sensitivities lead to different ERT observed breakthroughs. However, every TS in our experiment employed the same measurement sequence and obtained very similar datasets; therefore, we do not consider sensitivity an impairing factor in our study. Also, Miller, Routh, Brosten, and McNamare (2008) showed that independent inversions could work well if noise levels were low. We achieved a good model convergence with RMSEs in the interval 2.4–5.2%. As the saline solution infiltrates the column, in Figure 4, representative TSs illustrate the temporal changes in electrical resistivity. In order to visually emphasize the differences in electrical resistivity, we chose to show here TSs further apart in time; as the solution of increasing molarity was pumped into the soil, the resistivity model became more distinctive. Electrodes were only placed at 3-, 6-, and 9-cm height on the sample's exterior; hence, just the subvolume enclosed between them is shown. As time progresses, an increasing number of model cells display lower resistivities (indicated by blue rather than red colors). As the 5 M KCl saline solution reaches these regions of the soil volume, the pore solution will become more conductive, thus decreasing the bulk electrical resistance of the volume cell. Although this result is to be expected given the experimental settings, we aimed to estimate the change in electrical resistivity distribution across the whole volume more accurately. Therefore, the way pore structure and pore size distribution affected the changes observed was investigated further.

First, the samples' bulk changes in resistivity were quantified, and for every TS, the percentage of model cells that changed their corresponding resistivity over time by >10% of the initial value was calculated (Figure 5a). With time, more cell values are expected to change, hence the percentage will increase. Here, it is noticeable that the rate of such increase is different between the three groups (0.42, 0.34, and 0.17% min^{-1} for G1, G2, and G3, respectively). This could be explained by pore networks with different sizes and connectivities (Olsen et al., 1999). Also, the percentage of modified cell values reaches a stable state given enough time after the start of infiltration. This implies that saturation with the new saline solution is reached. Therefore, the different stable maximum percentage values (82, 44, and 24% for G1, G2, and G3, respectively) suggest samples with different porosities, as

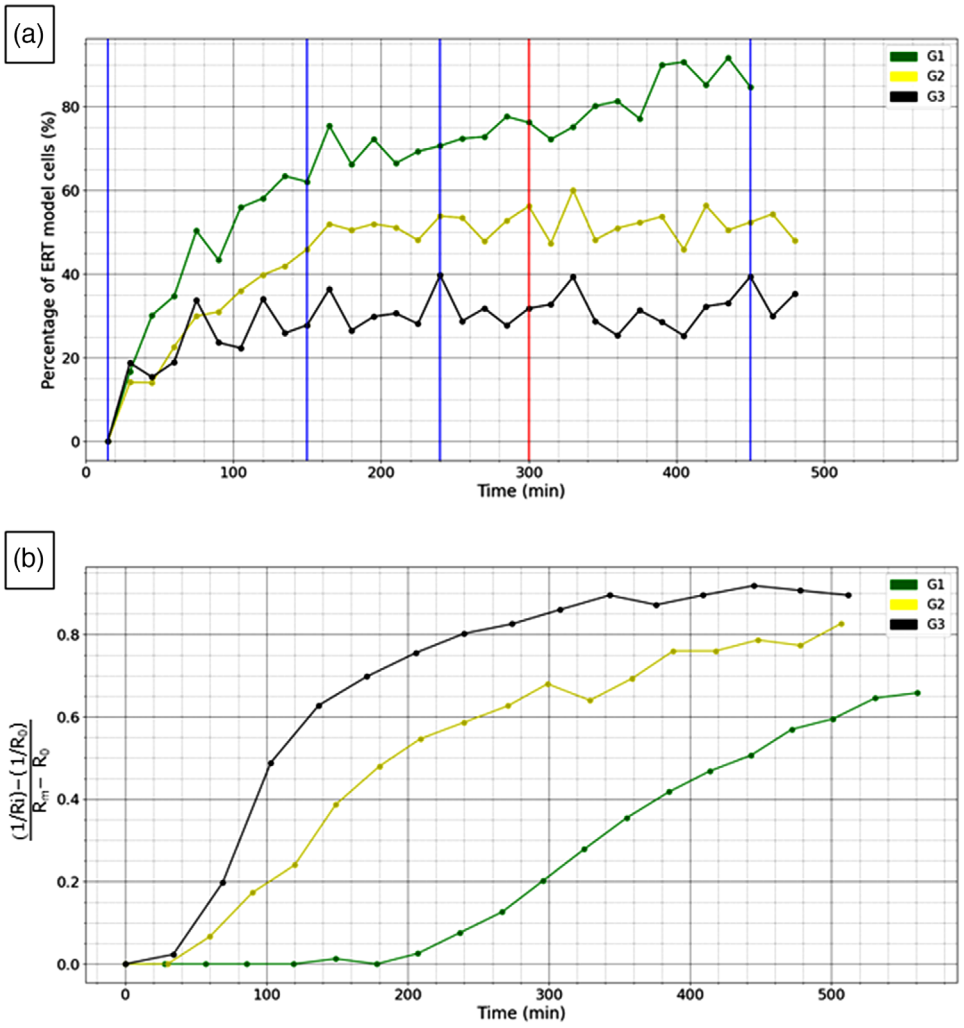

FIGURE 5 (a) Percentage of model cells which changed their resistivity by at least 10% with respect to time step (TS) 1. Red vertical line denotes TS 20. Blue vertical lines denote TSs corresponding to electrical resistivity tomography (ERT) models shown in Figure 4. (b) Effluent breakthrough of solute recorded presented as reduced concentrations. R is measured resistivity, R_i is initial conductivity, and R_m is the 5 M KCl tracer conductivity

a larger pore volume would allow the percolating saline solution to reach more cells. Analyzing the effluent's conductivity progression with time (Figure 5b), we observed that the higher the soil bulk density, the faster the effluent approaches the tracer's conductivity. A higher bulk density could imply that a less developed porosity leads to a smaller available pore fluid volume. Therefore, under the same constant rate of tracer injection, the concentration and thus the resistivity of the pore fluid changed in a shorter time and at a higher rate (G1 reached 0.9 in 340 min, G2 reached 0.78 in 380 min, and G1 reached 0.65 in 540 min).

3.2 | X-ray CT resolved parameters

Laboratory measurements and image analysis allowed us to estimate parameters that reflect the soil's internal structure (Figure 6). We compared such estimates between groups (G) in the attempt to observe the effect of compaction manifested through different levels of bulk density. Soils with higher bulk densities had a significantly ($p < .05$) lower porosity and pore connectivity density (Table 1 and Figure 6, a, d). Peyton, Haeffner, Anderson, and Gantzer (1992) also observed a proportionality between CT-derived macroporosity and soil bulk density. In terms of average pore size, there was not a significant difference ($p > .05$) between the three groups (Figure 6b). However, pore size distribution (Figure 6e) was different between the groups: G1 had the highest contribution to the overall pore volume coming from large pores (>1,000 μm), G2 had the highest contribution in the medium classes of pores (500–1,000 μm), and G3 had an overall reduced pore volume in all classes.

3.2.1 | Impact of soil structure on solution percolation

By modeling the pore network and its impact on solute transport, Vogel and Roth (2001) indicated that solute flow near

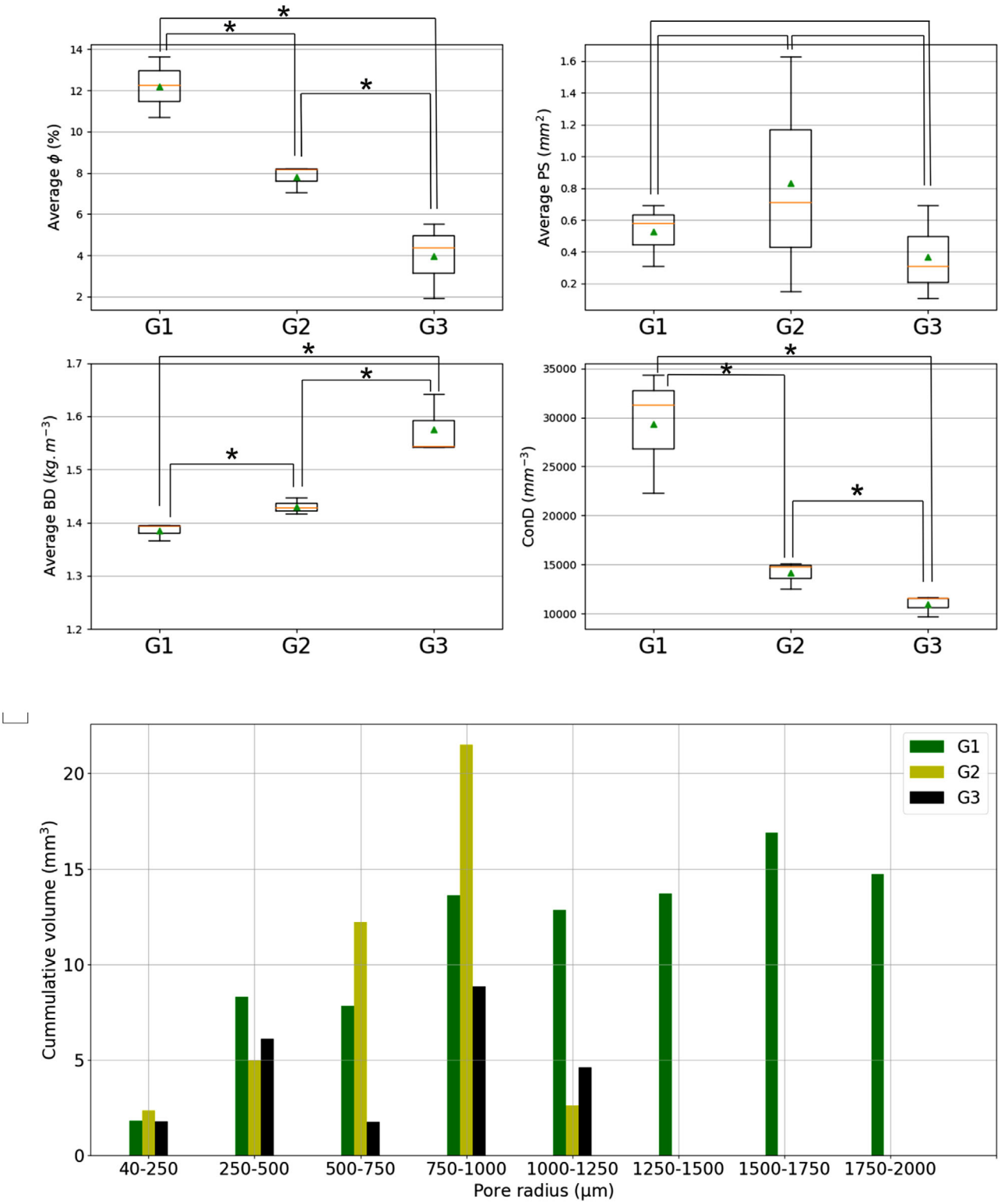

FIGURE 6 (a–d) Average values of pore structural parameters and their corresponding error bars as estimated from laboratory measurements (bulk density [BD]) and X-ray image processing (porosity [ϕ], pore size [PS], and connectivity density [ConD]). Orange lines indicate the median and green triangles the mean values. (e) Cumulative volume distribution across eight pore size classes corresponding to each bulk density group. Star symbols indicate statistically significant differences ($p < .05$) between the measurements

saturation was not affected by changes in pore radii, hence the main contributor to flow was the size of the pore network. With reference to the ERT results, soils with a higher porosity also had a higher percentage of resistivity model cells changed over time by the percolating solution (Figure 5). Garré et al. (2011) effectively used ERT to monitor soil moisture variability in soil columns. At the same scale, our result underlines ERT was also effective in delineating different soil solution percolation rates reflecting different soil bulk densities. Perret, Prasher, Kantzas, and Langford (2000) showed the complexity of pore structure in flow dynamics, revealing that dead-end branches or cavities as part of pore network determined low velocity through soil. Similarly here, the difference in resistivity rate of change between columns, given by the progressive proportion of resistive ERT model cells (Figure 5), can be viewed from the perspective of pore networks with different structures, as columns with higher rates of change also showed higher values of pore connectivities. Larger pore networks typically display higher connectivities (as it appeared in our case), but the shape of this relationship is not a linear and depends on soil type and management (Jarvis, Larsbo, and Koestel (2017). A well-connected network enables the infiltrating fluid to reach more regions of the soil volume, essentially allowing it to saturate more uniformly. Luo, Lin, and Schmidt (2010) established that X-ray CT-derived pore connectivity and macroporosity of a soil column drive its saturated hydraulic conductivity. In our study, compaction reduced the overall porosity and connectivity by effectively blocking pore channels that facilitate the connection between volumes of the pore network, thus also inhibiting the hydraulic conductivity. According to Rabot, Wiesmeier, Schlüter, and Vogel (2018), such inferences about connectivity of the pore network can in turn be used for the assessment of soil biota, as well as for water and gas transport.

3.3 | Relationship between porosity and change in electrical resistivity

3.3.1 | Qualitative assessment

In the previous subsection, we discussed the link between the pore structural parameters (Figure 6) and bulk electrical resistivity change (Figure 5) during the infiltration. We sought to explore the distribution of such changes across the 3D soil volume in greater detail. As data showed in Figure 5, by TS 20, the gradient of soil resistivity change has flattened. Therefore, by comparing the soil resistivity between TS 1 and TS 20, we effectively compare soil resistivity in the final stage with the soil resistivity in the incipient stage of the infiltration. As a consequence, the change in resistivity between TS 1 and 20 was calculated using Equation 7. In Figure 7, we compare the

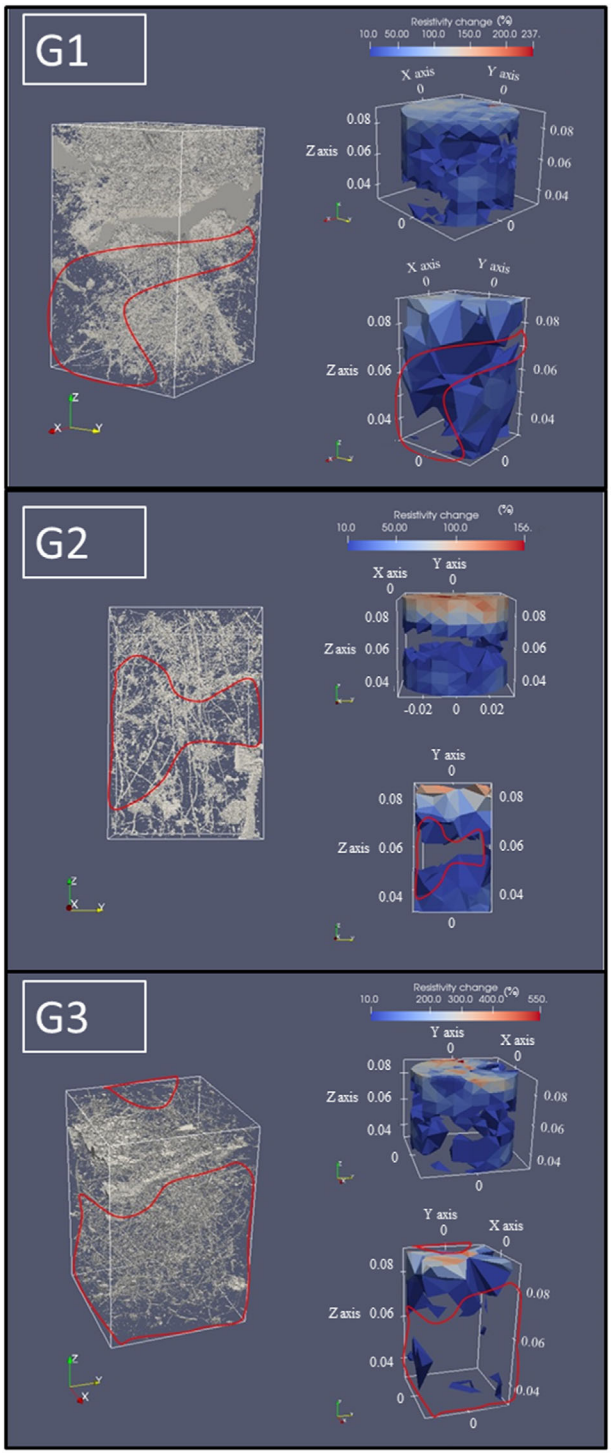

FIGURE 7 Left: Three-dimensional (3D) digital reconstruction of the pore volume as obtained following X-ray computed tomography (CT) image processing. Pore volumes correspond to one sample per bulk density group (shown in light gray). Red outlines indicate areas of underdeveloped porosity. Right: Electrical resistivity tomography (ERT) model cells (of the same samples shown on the left) that exhibited a change in resistivity >10% over the (top) whole column and (bottom) same region used for X-ray image processing

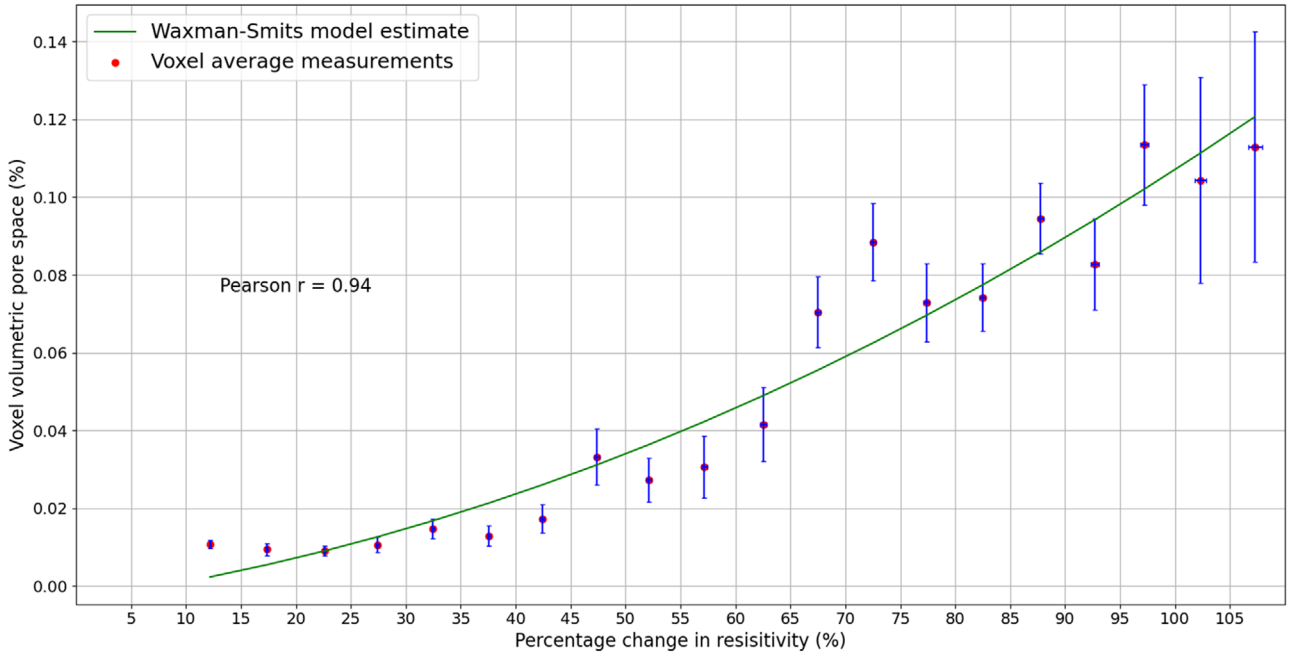

FIGURE 8 Relationship between the change in resistivity (computed between time step [TS] 1 and TS 20) and soil porosity for G1. The red dots represent the average measurements corresponding to the 128 voxels used to divide the soil volume. Blue error bars represent the standard error of the mean. The green line corresponds to the Waxman–Smits estimations obtained using Equations 6 and 7

distribution of pore space with the distribution of electrical model cells that had a change in resistivity >10% between TS 1 and 20. The values of resistivity change do not have the same upper boundary, as we wanted to show that the magnitude of change is indeed different between samples. On the 3D reconstructions of the pore space, we marked regions where pores were scarce, not present, or not resolvable (red outlines in Figure 7), and hence solution cannot percolate. Concurrently, in the same regions within the ERT models of resistivity change, a considerable (>10%) change in resistivity was not detected. A similar qualitative relationship between tomography outputs was observed by Olsen et al. (1999), where very resistive areas of ERT models were related by a denser material (e.g., stone) as revealed by X-ray CT images. Also, the available pore space across the sample decreases with increasing bulk density (a potential effect of compaction). A qualitative relationship between the two outputs is observable (Figure 7), even for the columns with the highest bulk density, which implies that providing pore connectivity, the contribution of pore solution salinity is considerable to the overall bulk electrical resistivity even when the pore space is reduced (G3 has porosity values of approximately a third of G1, Figure 6a).

3.3.2 | Quantitative assessment

A quantitative relationship between the two output models (resistivity change and pore spatial distribution) is required in order to be able to assess the impact that pore network structure has on the hydrodynamic behavior of soil. Estimated average resistivity changes for every subvolume voxel are verified against the existing pedophysical theory (Figure 8). The expected (model) resistivity change values were obtained using Equation 6 and X-ray CT estimated porosity. These are shown against the average pore space for the same voxels (Figure 8) in order to underline spatial correlation. The WS-estimated values correlated very well with the voxel average measurements, with a very high Pearson correlation coefficient (.94) between the two datasets. The standard error for the porosity error was larger for greater values of resistivity change. This is a spatially localized effect, but it reverts to the observations made earlier on the bulk resistivity evolution over time (Figure 5). Due to a larger available pore space, and hence more available pore solution, the homogenization process between the resident and the infiltrating solution takes longer. Also, macropore channels of similar volumes do not necessarily share the same pore connectivity, which imposes different susceptibilities to preferential flow (Jarvis et al., 2017). This, in turn, determines different homogenization rates and consequently different pore solution conductivities. Therefore, we postulate that for this soil type with its intrinsic physical properties, volumes of porosity larger than 10% are indistinguishable using time-lapse ERT. This implies that the overall structure of the soil directly influences the capability of our tomographic method (ERT) to distinguish between subvolumes of different porosities. For small changes in resistivity (<20%), we observed a disagreement between measurements and the WS curve. The

theoretical model predicts that lower porosities than the ones measured should account for the changes in electrical resistivity observed. However, in reality, pores are not perfectly interconnected; thus, a certain proportion of the pore space does not participate to the solution percolation in soils (Koestel et al., 2018; Perret et al., 2000). Therefore, a pore disconnected from the main flow path will contribute to an increase in total porosity but will fail to contribute to changes in electrical resistivity. On the other hand, the disagreement can be perceived as an overestimation of electrical parameters. The ERT monitors solute flow in near-real time, so during a TS acquisition, solute continued to move inside the column, which determined temporal smearing of electrical resistivity values (Slater et al., 2002).

Despite the assumption that changes in pore solution salinity would drive the resistivity changes, there was more certainty in our electrical model results when enhanced by complementary datasets (Everett, 2013), such as the soil columns' corresponding pore network. The X-ray scans show the spatial distribution of porosity across an individual soil sample in detail. The variability in electrical resistivity can now be explained based on the porosity variability across the sample. Furthermore, assuming that the porosity does not explain the resistivity variability, there must be other pedophysical factors responsible (e.g. organic material, increased salinity, and clay aggregates; Samouëlian et al., 2005), hence establishing a way to quantify their effect. It is however worth mentioning that this pedophysical model is only valid for bare soil. Therefore, if future studies consider soil with roots, additional uncertainty arises and needs to be addressed (Rao et al., 2020; Werban, Al Hagrey, & Rabbel, 2008). In addition, one must consider that an ERT model can show misleading variability due to factors contributing to its uncertainty, such as regularization, error model, and inversion related artifacts (different electrode contact impedance, finite electrode size). As the resolution used in this study only allows the quantification of macropores, the good fit between estimates and measurements suggests that macroporosity alone accounts for the detectable changes in electrical resistivity, hence the changes in pore solution concentration. Also, from the visualization of the pore network, even though it gives an appreciation of the soil hydraulic capability (e.g., water holding capacity, infiltration speed; Anderson et al., 2003; Tracy et al., 2015), we cannot infer details about the 3D pore solution percolation in near real time. Therefore, information from the two methods is complementary and enables a more comprehensive understanding of the soil hydrodynamic behavior.

4 | CONCLUSIONS

We have presented a methodology, which combines the strengths of two noninvasive tomographic methods, X-ray CT and ERT, in order to expose the hydraulic characteristics of a soil at different bulk densities. The former facilitated visualization and quantification of the soil pore architecture (distinguishing its size and shape), and the latter gave four-dimensional models representative of a tracer saline solution infiltration through the soil matrix.

We considered the effect that soil structure (from X-ray CT) had on solution percolation distribution over time (from ERT). Even though the soil columns had the same soil texture and the tracer had the same entry infiltration rate, the lower density soils revealed different percolation rates through faster spatial changes in electrical resistivity. Taken separately, X-ray CT could not describe or monitor the infiltration, and the resistivity ERT alone could not depict the fluid pathways due to its inversion model limitation. On the other hand, together, the X-ray pore structural parameters exposed a decreasing pore connectivity with increased bulk density, which explained the inhibited infiltration rates resolved through ERT bulk resistivity estimates. Furthermore, the spatial distribution of electrical resistivity change was collocated with areas densely populated by pores, indicating the accurate position of percolation channels. However, areas of porosity larger than 10% were indistinguishable using time-lapse ERT for our experimental setting, an effect of the overall structure of the pore network. Also, we obtained a good correlation (.94) between our data and estimates from a WS pedophysical model of electrical resistivity. A disagreement was observed for small changes in resistivity (<20%) attributed to temporal smearing. These results demonstrate the benefits of a conjunct application of ERT and X-ray CT to study soil hydrodynamics and underline the potential this methodology has to monitor and characterize hydrodynamic processes in the vadose zone.

ACKNOWLEDGMENTS

This work was supported by the Biotechnology and Biological Sciences Research Council, and the Natural Environment Research Council (Grant no. NE-M009106-1), through the Soils Training and Research Studentships (STARS) Centre for Doctoral Training grant to M.O. Cimpoiaşu. STARS is a consortium consisting of Bangor University, British Geological Survey, Centre for Ecology and Hydrology, Cranfield University, James Hutton Institute, Lancaster University, Rothamsted Research, and the University of Nottingham. In addition we would like to thank Brian Atkinson and Craig Sturrock (University of Nottingham, Hounsfield facility) for their help and advice with X-ray image processing, and Jim Whiteley (BGS) for his help with soil sampling and transportation.

CONFLICT OF INTEREST

The are no conflicts of interest regarding this research.

REFERENCES

Anderson, S. H., Wang, H., Peyton, R. L., & Gantzer, C. J. (2003). Estimation of porosity and hydraulic conductivity from X-ray

CT-measured solute breakthrough. *Geological Society, London, Special Publications*, *215*, 135–149. https://doi.org/10.1144/GSL.SP.2003.215.01.13

Archie, G. (1942). The electrical resistivity log as an aid in determining some reservoir characteristics. *Transactions of the AIME*, *146*, 54–62. https://doi.org/10.2118/942054-G

Cassiani, G., Kemna, A., Villa, A., & Zimmermann, E. (2009). Spectral induced polarization for the characterization of free-phase hydrocarbon contamination of sediments with low clay content. *Near Surface Geophysics*, *7*, 547–562. https://doi.org/10.3997/1873-0604.2009028

Cimpoiaşu, M., Kuras, O., Pridmore, T., & Mooney, S. (2020). A pedophysical relationship between X-ray computed tomography and electrical resistivity data. *Journal of Environmental and Engineering Geophysics*, *25*, 181–187. https://doi.org/10.2113/JEEG19-079

Cockx, L., Van Meirvenne, M., & De Vos, B. (2007). Using the EM38DD soil sensor to delineate clay lenses in a sandy forest soil. *Soil Science Society of America Journal*, *71*, 1314–1322. https://doi.org/10.2136/sssaj2006.0323

Doube, M., Kłosowski, M. M., Arganda-carreras, I., & Fabrice, P. (2010). UKPMC funders group BoneJ: Free and extensible bone image analysis in ImageJ. *Bone*, *47*, 1076–1079. https://doi.org/10.1016/j.bone.2010.08.023

du Plessis, A., Broeckhoven, C., Guelpa, A., & le Roux, S. G. (2017). Laboratory X-ray micro-computed tomography: A user guideline for biological samples. *GigaScience*, *6*(6). https://doi.org/10.1093/gigascience/gix027

Duliu, O. (1999). Computer axial tomography in geosciences: An overview. *Earth Science Reviews*, *48*, 265–281. https://doi.org/10.1016/S0012-8252(99)00056-2

Everett, M. E. (2013). *Near-surface applied geophysics*. Cambridge, UK: Cambridge University Press.

Farzamian, M., Monteiro, F. A., & Khalil, M. A. (2015). Application of EM38 and ERT methods in estimation of saturated hydraulic conductivity in unsaturated soil. *Journal of Applied Geophysics*, *112*, 175–189. https://doi.org/10.1016/j.jappgeo.2014.11.016

Furman, A., Arnon-Zur, A., & Assouline, S. (2013). *Electrical resistivity tomography of the root zone*. Madison, WI: SSSA.

Garré, S., Javaux, M., Vanderborght, J., Pagès, L., & Vereecken, H. (2011). Three-dimensional electrical resistivity tomography to monitor root zone water dynamics. *Vadose Zone Journal*, *10*, 412–424. https://doi.org/10.2136/vzj2010.0079

Grayling, K. M., Young, S. D., Roberts, C. J., de Heer, M. I., Shirley, I. M., Sturrock, C. J., & Mooney, S. J. (2018). The application of X-ray micro computed tomography imaging for tracing particle movement in soil. *Geoderma*, *321*, 8–14. https://doi.org/10.1016/j.geoderma.2018.01.038

Hamza, M. A., & Anderson, W. K. (2005). Soil compaction in cropping systems: A review of the nature, causes and possible solutions. *Soil and Tillage Research*, *82*, 121–145. https://doi.org/10.1016/j.still.2004.08.009

Hang, S. (2015). TetGen, a Delaunay-based quality tetrahedral mesh generator. *ACM Trans. on Mathematical Software*, 11. https://doi.org/10.1145/2629697

Hansen, P. (1992). Analysis of discrete ill-posed problems by means of the L-curve. *SIAM Review*, *34*, 561–580. https://doi.org/10.1137/1034115

Jarvis, N., Larsbo, M., & Koestel, J. (2017). Connectivity and percolation of structural pore networks in a cultivated silt loam soil quantified by X-ray tomography. *Geoderma*, *287*, 71–79. https://doi.org/10.1016/j.geoderma.2016.06.026

Johnson, T. C., Versteeg, R. J., Ward, A., Day-Lewis, F. D., & Revil, A. (2010). Improved hydrogeophysical characterization and monitoring through parallel modeling and inversion of time-domain resistivity and induced polarization data. *Geophysics*, *74*. https://doi.org/10.1190/1.3475513

Koestel, J., Dathe, A., Skaggs, T. H., Klakegg, O., Ahmad, M. A., Babko, M., … Jarvis, N. (2018). Estimating the permeability of naturally structured soil from percolation theory and pore space characteristics imaged by X-ray. *Water Resources Research*, *54*, 9255–9263. https://doi.org/10.1029/2018WR023609

LaBrecque, J., Miletto, M., Daily, W., Ramirez, A., & Owen, E. (1996). The effects of noise on Occam's inversion of resistivity tomography data. *Geophysics*, *61*, 538–548. https://doi.org/10.1190/1.1443980

Linde, N., Binley, A., Tryggvason, A., Pedersen, L. B., & Revil, A. (2006). Improved hydrogeophysical characterization using joint inversion of cross-hole electrical resistance and ground-penetrating radar traveltime data. *Water Resources Research*, *42*(12). https://doi.org/10.1029/2006WR005131

Loke, M. H., Chambers, J. E., Rucker, D. F., Kuras, O., & Wilkinson, P. B. (2013). Recent developments in the direct-current geoelectrical imaging method. *Journal of Applied Geophysics*, *95*, 135–156. https://doi.org/10.1016/j.jappgeo.2013.02.017

Luo, L., Lin, H., & Schmidt, J. (2010). Quantitative relationships between soil macropore characteristics and preferential flow and transport. *Soil Science Society of America Journal*, *74*, 1929–1937. https://doi.org/10.2136/sssaj2010.0062

Michot, D., Dorigny, A., & Benderitter, Y. (2001). Mise en évidence par résistivité électrique des écoulements préférentiels et de l'asséchement par le maïs d'un calcisol de beauce irrigué. *Earth and Planetary Sciences*, *332*, 29–36. https://doi.org/10.1016/S1251-8050(00)01498-1

Miller, C., Routh, P., Brosten, T. R., & McNamare, J. (2008). Application of time-lapse ERT imaging to watershed characterization. *Geophysics*, *73*, G7–G17. https://doi.org/10.1190/1.2907156

Muller, K., Vanderborght, J., Englert, A., Kemna, A., Huisman, J. A., Rings, J., & Vereecken, H. (2010). Imaging and characterization of solute transport during two tracer tests in a shallow aquifer using electrical resistivity tomography and multilevel groundwater samplers. *Water Resources Research*, *46*(3). https://doi.org/10.1029/2008WR007595

Musgrave, H., & Binley, A. (2011). Revealing the temporal dynamics of subsurface temperature in a wetland using time-lapse geophysics. *Journal of Hydrology*, *396*, 258–266. https://doi.org/10.1016/j.jhydrol.2010.11.008

Mwakanyamale, K., Slater, L., Binley, A., & Ntarlagiannis, D. (2012). Lithologic imaging using complex conductivity: Lessons learned from the Hanford 300 area. *Geophysics*, *77*, E397–E409. https://doi.org/10.1190/geo2011-0407.1

Odgaard, A., & Gundersen, H. (1993). Quantification of connectivity in cancellous bone, with special emphasis on 3-D reconstructions. *Bone*, *14*, 173–182. https://doi.org/10.1016/8756-3282(93)90245-6

Olsen, P. A., Binley, A., & Tych, W. (1999). Characterizing solute transport in undisturbed soil cores using electrical and X-ray tomographic methods. *Hydrological Processes*, *13*, 211–221. https://doi.org/10.1002/(SICI)1099-1085(19990215)13:2/3c211::AID-HYP707/3e3.0.CO;2-P

Otsu, N. (1979). A threshold selection method from gray-level histograms. *IEEE Transactions on Systems, Man, and Cybernetics*, *9*, 344–349. https://doi.org/10.1109/TSMC.1979.4310076

Perret, J., Prasher, S. O., Kantzas, A., & Langford, C. (2000). A two-domain approach using cat scanning to model solute transport in soil. *Journal of Environmental Quality*, *29*, 995–1010. https://doi.org/10.2134/jeq2000.00472425002900030039x

Peyton, R. L., Haeffner, B. A., Anderson, S. H., & Gantzer, C. J. (1992). Applying X-ray CT to measure macropore diameters in undisturbed soil cores. *Geoderma*, *53*, 329–340. https://doi.org/10.1016/0016-7061(92)90062-C

Rabot, E., Wiesmeier, M., Schlüter, S., & Vogel, H. J. (2018). Soil structure as an indicator of soil functions: A review. *Geoderma*, *314*, 122–137. https://doi.org/10.1016/j.geoderma.2017.11.009

Rao, S., Lesparre, N., Orozco, A. F., Wagner, F., & Javaux, M. (2020). Imaging plant responses to water deficit using electrical resistivity tomography. *Plant and Soil*, *454*, 261–281. https://doi.org/10.1007/s11104-020-04653-7

Romero-Ruiz, A., Linde, N., Keller, T., & Or, D. (2018). A review of geophysical methods for soil structure characterization. *Reviews of Geophysics*, *56*, 672–697. https://doi.org/10.1029/2018RG000611

Rücker, C., & Günther, T. (2011). The simulation of finite ERT electrodes using the complete electrode model. *Geophysics*, *76*, F227–F238. https://doi.org/10.1190/1.3581356

Samouëlian, A., Cousin, I., Tabbagh, A., Bruand, A., & Richard, G. (2005). Electrical resistivity survey in soil science: A review. *Soil and Tillage Research*, *83*, 173–193. https://doi.org/10.1016/j.still.2004.10.004

Schindelin, J., Arganda-Carreras, I., Frise, E., Kaynig, V., Longair, M., & Pietzsch, T. (2012). Fiji: An open source platform for biological image analysis. nature methods. *Nature Methods*, *9*, 676–682. https://doi.org/10.1038/nmeth.2019

Slater, L., Binley, A., Versteeg, R., Cassiani, G., Birken, R., & Sandberg, S. (2002). A 3D ERT study of solute transport in a large experimental tank. *Journal of Applied Geophysics*, *49*, 211–229. https://doi.org/10.1016/S0926-9851(02)00124-6

Tracy, S. R., Daly, K. R., Sturrock, C. J., Crout, N. M. J., Mooney, S. J., & Roose, T. (2015). Three-dimensional quantification of soil hydraulic properties using X-ray computed tomography and image-based modeling. *Water Resources Research*, *51*, 1006–1022. https://doi.org/10.1002/2014WR016020

Vogel, H. J., & Roth, K. (2001). Quantitative morphology and network representation of soil pore structure. *Advances in Water Resources*, *24*, 233–242. https://doi.org/10.1016/S0309-1708(00)00055-5

Waxman, M., & Smits, L. (1968). Electrical conductivities in oil-bearing shaly sands. *Society of Petroleum Engineers Journal*, *243*, 107–122. https://doi.org/10.2118/1863-A

Werban, U., Al Hagrey, S. A., & Rabbel, W. (2008). Monitoring of root-zone water content in the laboratory by 2D geoelectrical tomography. *Journal of Plant Nutrition and Soil Science*, *171*, 927–935. https://doi.org/10.1002/jpln.200700145

Wildenschild, D., Hopmans, J. W., Vaz, C. M. P., Rivers, M. L., & Rikard, D. (2002). Using X-ray computed tomography in hydrology: Systems, resolutions, and limitations. *Journal of Hydrology*, *267*, 285–297. https://doi.org/10.1016/S0022-1694(02)00157-9

Wildenschild, D., & Sheppard, A. P. (2013). X-ray imaging and analysis techniques for quantifying pore-scale structure and processes in subsurface porous medium systems. *Advances in Water Resources*, *51*, 217–246. https://doi.org/10.1016/j.advwatres.2012.07.018

How to cite this article: Cimpoiaşu MO, Kuras O, Wilkinson PB, Pridmore T, Mooney SJ. Hydrodynamic characterization of soil compaction using integrated electrical resistivity and X-ray computed tomography. *Vadose Zone J.*. 2021;1−15. https://doi.org/10.1002/vzj2.20109